Experimental and simulated heating in nanocrystalline diamond charge exchange injection films using an electron beam to mimic SNS conditions

Leo Saturday [a], Chris Luck [c], Leslie Wilson [b], Jason D. Fowlkes [b], Philip D. Rack [a,b], Nicholas J. Evans [c]

[a] *University of Tennessee at Knoxville, Knoxville, TN 37996, United States of America*
[b] *Center for Nanophase Materials Sciences, Oak Ridge National Laboratory, Oak Ridge, TN 37830, United States of America*
[c] *Research Accelerator Division, Oak Ridge National Laboratory, Oak Ridge, TN 37830, United States of America*

Keywords:

Charge exchange injection; Nanocrystalline diamond; Electron beam mimic; Stripper foil; Foil failure; Sublimation

Abstract:

Nanocrystalline diamond (NCD) foils have been in use at the Spallation Neutron Source as primary stripper foils for charge exchange injection since the machine's inception. NCD's low atomic number leads to reduced beam scattering while still being easy to handle, as opposed to even lighter elements. NCD foils also have the benefit of being free-standing, and rigid when grown under the right conditions to minimize residual stresses. This study overviews a method to mimic the Spallation Neutron Source (SNS) beam and characterize thermally driven failure of NCD foils. To do this, a foil test stand was developed with in situ diagnostics that tracks signs of foil sublimation and thinning. The foil test stand's electron beam is equated to the SNS beamline by comparing peak deposited energy densities for both beams. Post-mortem testing is also conducted to help elucidate changes the NCD foils undergo during exposure to the beam. A COMSOL simulation was also developed as a method to assess potential future changes to the NCD film and predict how changes to beam conditions will effect foil temperatures. This method allows for examination of the NCD foil's thermal limits and can be used to assess future changes to SNS stripper foils.

Acknowledgement:

This work was supported by the DOE office of Science User Facilities. LS, LW, and NE are supported through funding for the Spallation Neutron Source. SNS is managed by UT-Battelle, LLC, under contract DE- AC05-00OR22725 for the U.S. Department of Energy. Foil synthesis, certain post-mortem testing, and modeling were conducted at the Center for Nanophase Materials Sciences, which is also a DOE Office of Science User Facility. Additionally, the authors would like to thank Jeff Holmes for simulations of the SNS beam/foil interaction, and Willem Blokland for operational data from the SNS foil pyrometer.

Introduction

Charge exchange injection (CEI) is a process where a beam of H- ions are converted to H+ ions to increase the phase space density of a beam for the operation of high-power proton sources such as the Spallation Neutron Source (SNS) at Oak Ridge National Laboratory. This charge conversion is traditionally achieved through the interaction of the H- beam with either a solid material called a stripper foil, or a jet of gas, or liquid [1]. Beam scattering due to CEI scales with both atomic number and thickness of the stripping medium [2]. Carbon based materials are frequently used as stripper foils for the CEI process [3]. Carbon's low atomic number results in reduced scattering of the interacting charged particle beam compared to higher atomic number alternatives. Additionally, many forms of carbon have high thermal conductivity and enable better heat dispersion. Carbon stripper foils are generally limited by their lifetime when exposed to beam, which is shortened by a combination of thermal and mechanical failure. In order to extend the stripper foil lifetime and help mitigate some of these failure mechanisms, SNS has developed a nanocrystalline diamond foil [4] with improved mechanical and thermal stability compared to amorphous carbon foils. Though foils usually perform very well, and are often removed from service before failure, when foils do fail, graphitization and subsequent deformation of the SNS foils are the primary failure mechanism. This deformation typically leads to higher beam loss, or unpredictable behavior related to small changes in foil positioning that is unacceptable for operations, rather than catastrophic failure. However, sublimation has been observed during SNS operation under non-ideal beam conditions, and as beam power density increases with future SNS upgrades, sublimation is expected to occur and could potentially be a problem for reliable operation. While sublimation of the SNS nanocrystalline diamond foils has been observed, an explicit examination of the limits of the SNS NCD foils has not been thoroughly conducted.

Previous work has been done to examine the lifetimes and temperatures for carbon stripper foils. Stripper foil lifetime estimates have been proposed in other works with regards to radiation and evaporation [5] as well as foil thickness [6]. Additionally, the temperatures generated during charge exchange injection on the foil has been simulated [7– 10] and experimentally measured [11]. Electron beams have also been utilized to mimic and examine the heating effects on stripper foils [6, 12]. Recently, diagnostics were developed and implemented for in situ monitoring of pinhole formation and thinning of stripper foils [13]. In this work we examine the thermal limits of the SNS NCD stripper foils.

One of the limiting factors in electron stripper foil research is the ability to dedicate beam time to test and change out stripper foils in the SNS beam line. In order to expedite testing, an electron beam Foil Test Stand (FTS) was developed to emulate the heating caused by the SNS beam [14]. The FTS mimics the energy deposition into the foil by equating the stopping power of the SNS H^- beam to an equivalent electron beam stopping power. This method does not mimic the radiation damage caused by high energy protons, however, from SNS operational experience, foil lifetime is believed to be limited by sublimation due to heat. Several *in situ* diagnostics have been added to the system for *in operando* monitoring to elucidate critical steps in the foil failure. Here we overview the FTS system and correlate *in situ* diagnostics and post-mortem characterization to the thermomechanical failure of nanocrystalline diamond foils under electron beam conditions that mimic the SNS beam.

Methods

Nanocrystalline diamond (NCD) films were first fabricated for test- ing at the Center for Nanophase Materials Sciences. Samples were deposited in DiamoTek 700-6 Microwave Plasma CVD system using parameters as described in previous literature [15]. Experimentally, the deposited material usually varies around 0.1 mg. When accounting for the exposed surface area of the silicon chip, this deposition corresponds to an areal density of 357 to 372 $\mu g/cm^2$ and a thickness ranging between 1.23 and 1.28 µm for the FTS samples and a representative SNS stripper foil. After diamond synthesis and the subsequent etching/release from the substrate, the ∼1 µm thick nanocrystalline diamond samples were mounted in the foil test stand (FTS) for test- ing. An overview of the FTS along with the associated hardware and measurements are illustrated in Fig. 1.

FTS Hardware

Foils are first mounted to the vertical and rotational multi-motion feedthrough that is illustrated in the photograph in Fig. 1(a) and schematic in (b). Up to four foils can be mounted in the system and the samples are able to be rotated 360°. This allows the foil to be positioned 30° from normal to the electron beam, emulating the interaction angle of the SNS H^- beam with the stripper foil. The electron beam isgenerated with a Kimball Physics electron source that generates an approximately Gaussian beam profile. The end of the electron gun is positioned approximately 120 mm from the foil. Along the electron gun diameter a Faraday cup is mounted on the other side of the chamber that has a 3 mm diameter current limiting aperture. A FLIR camera is attached normal to the face of the foil. A gas analyzer is also attached to a port and is shielded by an optically dense baffle. Typical graphs of the gas analyzer, FLIR temperature measurements, emission current, and Faraday cup current are shown in Figs. 1c, 1d, and 1e for the irradiation of a previously unexposed spot. Lastly a high definition camera is mounted outside of a transparent vacuum window for high resolution imaging of the foil before and after exposure. The vacuum pressure is held in the 10^{-8} to the 10^{-9} torr range and fluctuates during foil tests.

FTS Measurements

Once mounted on the FTS multi-motion feedthrough, the stripper foils are exposed to an electron beam that, as described below, has comparable energy deposition in the carbon foil as the 1.0 GeV, 1.4 MW H^- + H^+ beam. During the electron beam exposure, the FLIR IR camera captures the two dimensional temperature profile of the foil at a calibrated exposure. The FLIR camera has a temperature accuracy of ±1% assuming an accurate object emissivity. Note that to obtain the absolute temperature the image must be calibrated against the spot's emissivity. The temperature profile and maximum temperature is tracked and reported throughout each run. It is important to note that since the emissivity changes during beam exposure, the temperature measurements are slightly inaccurate in the early frames when the electron beam first interacts with the foil. This inaccuracy is due to the emissivity change of the foil during initial graphitization [16]. During beam exposure the residual gas analyzer is set to track specific mass-to-charge ratios (Fig. 1(c)) that are expected to outgas or sub- lime from the foil. Some of the specific mass-to-charge ratios that are recorded look for H_2O that can desorb from surfaces due to increased temperature, and carbon/carbon byproducts that can be the results of sublimed free carbon. The Faraday cup is used to monitor the un- scattered beam current which can be correlated to the FLIR camera temperature reading (Fig. 1(d)) and the emission current of the electron gun (Fig. 1(e)). The foil irradiation shown in Fig. 1c, d, and e is on a previously unirradiated spot. When irradiating a fresh spot, the partial pressure spikes, and the emission current drops by approximately 10%, which subsequently decreases the foil temperature. The drop in emission current and foil temperature is attributed to electron beam and thermally stimulated desorption of physisorbed gas-phase products on the diamond foil, which when released subsequently interact with the electron gun cathode. The high definition camera is used to image the foil *in situ* as well as collect post irradiation photos of the exposed area. The foil holder is also used as a beam scraper, which is incrementally raised so the measured Faraday cup current change as a function of position could be recorded, which was used to re-construct the beam profile [see supplemental information for details].

SNS Equivalent current

The equivalent SNS and FTS peak beam currents were estimated by equating the energy deposited in the nanocrystalline diamond foil for both beams via the relative stopping powers of the particles and the beam profiles. As will be described below, the emission current and beam profiles are measured for the 30 keV electrons and the electron stopping power for a 30 keV electron is 8.6290 MeV cm^2/g. The SNS peak energy deposited is estimated using the stopping power of a car- bon foil for a proton and 2 electrons at their relative energies assuming a 1.0 GeV H^- beam. The recirculating proton beam is also accounted for as it strikes the foil on average 4 to 5 additional times. The peak current including recirculating beam is estimated from realistic ORBIT simulations [17] of the entire injection process that includes all relevant effects. Stopping power values for the convoy electrons and protons at their respective energies are 1.761 MeV cm^2/g and 1.946 MeV cm ^{2}/g, respectively. The simulated SNS beam profiles are briefly described in the supplemental information, where it is noted that the H- and H+ distributions are slightly offset. Thus, accounting for the beam profiles, one can approximate the equivalent peak SNS and FTS currents based on the peak energy deposited per area for each beam, where:

$$1.65 \times i\,(FT\,S_{e-}) = i(SNS_{4.5H^{+}+H^{-}})$$

The reader should note that this equivalence assumes the current 1.0 GeV SNS proton beam energy. After the Proton Power Upgrade, SNS will be capable of a 1.3 GeV beam, and the energy deposition of both protons and electrons will decrease by about 5% for foils of similar thickness.

Post mortem testing

After the foils are tested in the FTS, post mortem testing was also performed. Raman spectra were taken of the exposed foils in multiple areas (shown later). Polycrystalline diamond is commonly examined and identified using Raman spectroscopy and gives insight to the carbon phases present in the sample [18,19]. Scanning electron microscopy (SEM) was used to take surface images of the exposed areas and gives insight into the potential causes of failure in the foil. Additionally, a black body source is used to measure the emissivity of the foil's exposed and unexposed area. To do this the foil is used as a filter between the black body source and the FLIR IR camera. This allows us to determine the transmission from the exposed spots and calculate the emissivity [16].

Simulation

Finite element methods were used to model heat flow in the stripper foils. A Monte Carlo simulation was first performed to better estimate the energy deposition profile of the electron beam interacting with a carbon foil at a density of 2.9 g/cm^3 and an areal density of 362.5 µg/cm^2 which corresponds to a foil thickness of 1.25 µm. The Monte Carlo algorithm used to generate individual electron trajectories has been described previously [20] and is based on the algorithm developed by Joy [21]. The simulation of electron exposure was 3D with respect to the electron beam — target interaction. Multiple simulations were executed to study the implications of changes in sample thickness and the sample tilt orientation with respect to the beam. In each study, the inelastic energy loss in the z-coordinate, i.e., parallel to the beam trajectory, was compiled as a function of the z-coordinate (depth). The total stopping power at 30 keV was determined to be 9.24 MeV cm^2/g, which is similar to the value of 8.575 MeV cm^2/g given in the NIST ESTAR database [22], assuming a constant energy loss for 30 keV electrons in carbon. Subsequently, these profiles served as an energy generation term in the heat diffusion partial differential equation that was solved using a finite element method solver. The energy loss profile was scaled to the FTS current distribution and used as the heat source for the COMSOL model to simulate the thermal evolution of the stripper foils during electron beam exposure [23]. The percentage of inelastic energy contributing to heat by the beam (ε) was adjusted in order to get a correct fit between experiments and simulations. As mentioned above, the electron beam profile was measured using the foil holder, which was progressively moved to measure the collected current. The derivative of this profile was then fit to a 1D integral of a 2D Gaussian ring function and used for the simulated beam profile.

Thermal conductivity and specific heat values are temperature de- pendent and need to be considered in the thermal model due to the high temperature range experienced under the electron exposure. It should be noted that graphitization occurs in the temperature region above 1473 K [24] and could influence these terms. The specific heat of carbon allotropes seem to be fairly consistent with minimal variance between its forms [25–27]. Therefore specific heat values from previous literature, up to 3000 K, were used to estimate temperature dependent specific heat [27]. Thermal conductivity, however, can vary significantly between different diamond [28] and graphite [29–31] samples. This is problematic as the evolution of the NCD graphitization is not specifically known. For this model, a piecewise function was constructed for the thermal conductivity of un-graphitized foils. As NCD has a fairly flat curve at room temperature, thermal conductivity was assumed to be constant and assigned the previously measured 10 W/(m*K) [15] until it reaches 1300 K. From 1300 to 1500 K the thermal conductivity transitions linearly to an isotropic polycrystalline graphite estimation; at temperatures greater than 1500 K a function that fits high temperature polycrystalline graphite is used. As will be justified below, for the pulsed simulations, the thermal conductivity of the central graphitized spot is assumed to be polycrystalline graphite. See supplemental information for specific heat and thermal conductivity temperature dependent functions used in the simulations.

Results and discussion

The main signatures of sublimation in the FTS are changes in temperature and Faraday cup current normalized to the emission current. Foil thinning leads to less scattering of the primary electron beam and thus an increase in the measured Faraday cup current. Additionally, as the foil thins due to sublimation, the electron energy deposited in the foil decreases, and consequently the temperature decreases. Thus, the Faraday cup and FLIR IR camera readings are the primary indicators of sublimation *in situ*. However, changes in the electron gun emission current can also occur during the foil testing, thus in order to compensate for changes in the electron gun current, the Faraday cup current is normalized by the emission current. Fig. 2 is a plot of the ratio of the Faraday cup current and the emission current versus time for two different pulsed emission beam currents. As the emission current increases, the sublimation rate increases as evidenced by the steeper slope of the normalized Faraday cup current versus time plot.

By comparing the temperature and normalized Faraday cup current of various exposure currents, three different regimes for the foils can be observed and are shown in Fig. 3a. First we expose a fresh foil to a 200 μA continuous wave (CW) emission current. At this current, the foil rapidly graphitizes and the increased emissivity causes a decrease in temperature. The absolute temperature measurement in this early region is not reliable due to the changing emissivity. The temperature decrease saturates near 300 s and during this stage, the normalized Faraday current only slightly increases. We then increase the emission current to 300 μA, and while the temperature instantly rises ~90 K, the normalized Faraday cup current initially equals the final value in region 1 (i.e. the fraction of emission to collected currents for the end of region 1 and beginning of region 2 are the same). The normalized Faraday cup current in region 2 increases and there is a slight concomitant decrease in peak temperature. The slope of the normalized Faraday cup current versus time suggests that sublimation rate is initially high and during the second 300 s exposure begins to taper and nears saturation at 600 s; the thinning in region 2 causes a net change of ~65% in the normalized Faraday current and an ~10 K decrease in temperature. In the third region, the emission current is increased again to 380 μA, which causes an instantaneous increase of ~120 K in temperature. During the 300 s exposure the temperature decreases significantly (~90 K) concurrent with an increase in normalized Faraday cup current, indicating heavy sublimation and a potential hole formation in the film. Note the graphite vapor pressure is ~4 × 10^{-8} Torr at 2000 K, thus sublimation of the graphitized foil is reasonable in these electron exposure conditions. Fig. 3b shows the NCD foil after irradiation. The graphitized region can be clearly seen along with the deformations caused to the surrounding foil.

Post mortem testing was also conducted to elucidate the changes occurring to the nanocrystalline diamond foils. Emissivity measurements were conducted using a black body source as described in section 3.2.2.2 of Barrowclough's dissertation [16] and used for FLIR measurements. Raman spectra were taken in the relative regions shown in Fig. 4. The results show the central area 1 has sharp peaks at 1325 and 1585 cm^{-1}, which are associated with strong crystalline graphite and diamond vibrations, respectively. Additionally, peaks around 2700 and 2900 cm^{-1} are observed and are similar to peak patterns found in carbon nano-onions [32]. The second region has discernible peaks at 1335 and 1595 cm^{-1} which are broader than region 1, suggestive of potentially a more disordered material with defects [33] or a shift to smaller grain size of the sample [34]. Region 3 is an unexposed region and has two peaks at 1330 and 1565 cm^{-1}; the peaks are broad and indicative of the nanocrystalline diamond and an amorphous phase of carbon. Additionally, SEM imaging was conducted on these foils in order to directly observe potential failures and can be seen in Fig. 4. Holes in the foil caused during exposure are seen in the SEM images. This helps to determine that the cause of the failure is sublimation rather than mechanical failure. Hole formation, noted in the yellow box, is attributed to excessive sublimation at the hot spots of the electron gun, as there is no visible stress accumulation in the area. However, large wrinkles have also formed along ridge lines in the exposed area. These wrinkles are attributed to mechanical stress accumulation caused during graphitization.

Beam line temperature data was obtained from the SNS with an accuracy of ±2.5%. With a 1.4 MW, 1 GeV beam the peak temperature was measured to be 1750 K. This was taken using a dual band pyrometer and is an emissivity independent reading [11,35]. The beam power was gradually increased in steps up to 1.4 MW. The temperature versus time profile is plotted in Fig. 5. The data has an artificial dip when the temperature goes below 1200 K, which is an artifact of the measurement method. 1750 K measurements were obtained on the FTS with a current of 750 μA, which is also shown in Fig. 5. The FTS measurement was conducted during a 10 s exposure on a spot that was first conditioned with 10 s sequential exposures of 250 and 500 μA beams. The cooling curves differ between the two beams and is likely an effect of the difference in the beam profiles and sizes. Thus, while the peak temperature achieved is the same, larger spot sizes can result in a slower thermal decay (see supplemental information for details).

To correctly model the electron beam heating and equate the FTS and SNS beams, we measured the spot size/shape of the electron beam to determine the peak current density. This value was determined by blocking the beam from the Faraday cup with a piece of titanium and slowly raising the titanium in 25 μm steps to progressively expose the beam to the Faraday cup. The derivative of this data was taken with a Savitzky–Golay filter and the projection of a Gaussian ring-shaped beam was used to fit the profile. This determination was made with the assumption of a radially symmetric beam. Radial symmetry is a reasonable assumption based on phosphor screen images taken at low intensity which cannot be used to determine the profile at higher intensities. We used the following model for a Gaussian ring beam profile

$$f(x,y) = \frac{2\sigma^2}{\sqrt{x^2+y^2}}\left(\exp\left(\frac{2R\sqrt{x^2+y^2}-x^2-y^2-R^2}{2\sigma^2}\right)\right.$$
$$\left.-\exp\left(\frac{-2R\sqrt{x^2+y^2}-x^2-y^2-R^2}{2\sigma^2}\right)\right)$$

where σ is the standard deviation and R is the Gaussian ring radius. This allowed an estimation of the beam shape to be extracted with a ring radius of 220 μm and a standard deviation value of 75 μm. The beam profile peak current densities of the FTS are estimated from this beam shape.

COMSOL simulations were performed by emulating an electron beam at 30 keV, varying current, and the beam shape parameters previously determined. In order to estimate the percentage of deposited beam energy that goes into heating (ε), a continuous wave (CW) experiment was first simulated. A CW beam was chosen to make sure that good correlation was obtained between experimental and simulated data before emulating the pulsed beam. Comparison with a CW beam also verifies the correct thermal conductivity has been assumed for this temperature range, as shown in Fig. 6a. Using the temperature dependent physical parameters, electron beam profile discussed above, and an integrated beam current of 200 µA, the CW thermal excitation curve was best fit with a simulation assuming an ε of 74%. An ε of 74% is not unreasonable due to the many inelastic channels through which electrons can lose energy. In a recent study, the heating due to inelastic energy loss was estimated in ultrathin membranes (22-61 nm), and the accuracy of measuring the inelastic energy loss was on the order of 20% consistent with our estimation of ε [36].

Using the determined ε for the CW experiment and simulations, pulsed simulations were conducted using a 750 µA, that matched the SNS peak temperature, and 1 mA beams. Both simulations were pulsed at 1 ms and 60 Hz (6% duty cycle) and compared against experimental data, shown in Figs. 6b and 6c, respectively. A peak current density of 1.98 mA/mm^2 is realized in the 750 µA and 2.64 mA/mm^2 in the 1 mA experiments based on the beam profiles. In the 750 µA experiment versus simulation comparison the simulated foil has a maximum temperature of 1800 K and is very close to the experimentally observed peak temperature of 1746 K. For these exposures there is no experimentally observed sublimation in agreement with the graphite vapor pressure curve [37]. The 1 mA beam simulation results in a peak temperature of 2160 K, which is also in good agreement with the average peak experimental temperature of 2080 K. This difference between simulation and experiment can be partially due to sublimation that occurs in the foil or, of course, standard error in the experimental versus simulations values used. As the sample sublimes, the thickness decreases and the energy deposited decreases which, as shown in Fig. 3, decreases the effective temperature of the foil. The material loss is not accounted for in the simulation and could cause discrepancy with the experimental results.

Foil degradation was observed during the 1 mA experimental FTS runs as the normalized Faraday cup current increased during exposure and as-revealed via post mortem pictures of the foil. The 750 µA beam showed no signs of failure and was determined to be a stable regime. By using the SNS design beam parameters, the 750 µA and 1 mA beams correspond to an SNS peak energy deposition density per pulse of $4.26 * 10^{10}$ MeV/mm^2 and $5.68 * 10^{10}$ MeV/mm^2 respectively. We used ORBIT simulations of an optimized injection to estimate the proton and electron hit number density on the foil during well-tuned SNS operation and then use tabulated energy deposition values to estimate the peak energy density per pulse. For a 362 ug/cm^2 foil the predicted peak energy deposition per pulse is $1.75 * 10^{10}$ MeV/mm^2, 2.43 times lower than the 750 µA case. Based on this, the SNS should safely be able to run 3.36 MW at 1.0 GeV using foils currently used during operation. Simulations of the 2.8 MW, 1.3 GeV scenario assumed for the future upgrades to the facility produce peak energy deposition of $2.93 * 10^{10}$ MeV/mm^2, 1.45 times lower than the 750 µA case. At 1.3 GeV powers of 4.06 MW should also be comfortable. The 1 mA limit corresponds to powers of 4.55 MW and 5.43 MW at 1.0 GeV and 1.3 GeV respectively, but this represents the regime where we see foil failure. One should note the foil thickness assumed here is slightly larger than necessary but corresponds roughly to the current operational situation. The thickness could be reduced another 10% or more if more margin is needed. Scaling the power in this way is reasonable, but requires some caveats as the actual peak power deposited depends on many parameters including the injected H^- and recirculating proton beam profiles which can change during tuning of the beam. However, as demonstrated in the FTS data, the equivalent energy deposition density values can be used to determine when the foils are approaching an unstable regime where foil failure will occur.

To understand the sensitivity of the COMSOL simulation results, a sensitivity analysis was conducted. For the baseline of this analysis a 750 µA beam with an ε of 74%, ring radius of 220 µm, Gaussian standard deviation value of 75 µm, and graphitized emissivity of 0.9 was used. The ring radius, Gaussian standard deviation value, current, ε, emissivity, and thermal conductivity were each individually increased by 10% and the resultant peak temperatures were simulated and compared. Table 1 is a summary of the changed simulation parameters and the resultant simulated peak temperature and the change in peak temperature. Of course, changing the current and ε have the same effect of linearly increasing the energy deposited and this had the strongest effect on temperature. The beam's ring radius had the next largest effect. The rest of the changed variables had minimal impact and resulted in less than 23 K (1.3%) deviation in the peak temperature.

In addition to helping to understand the limits of what SNS standard foils can withstand, the COMSOL model will also be able to assist in future improvements and revisions to foils. By being able to rapidly simulate different geometries and changing physical properties in the charge injection stripper foils, this method can help to direct foil improvements in the most beneficial directions. Fast simulations coupled with previous literature on varying NCD growth recipes and the resultant properties, will hopefully lead to improved future stripper foils.

Conclusion

An electron beam mimic of the charge exchange injection stripper foil has been developed and the equivalent power density of the H-ion and the electron beam has been calculated. An equivalent beam of 30 keV electrons penetrating a nanocrystalline diamond stripper foil has been experimentally measured and simulated via a COMSOL thermal model. The Faraday cup and FLIR IR camera show indications of sublimation that can be tracked throughout the exposure of the foil. Postmortem testing was also conducted in order to give insight into the changes that occurred during the stripper foils' exposure to the electron beam. The methods developed and used in this paper allow for testing of stripper foils on a much faster time scale than would be possible in the main SNS beamline. Utilizing these methods while varying synthesis parameters for the nanocrystalline diamond growth, will lead to a better understanding and potential improvement in stripper foil failure limits.

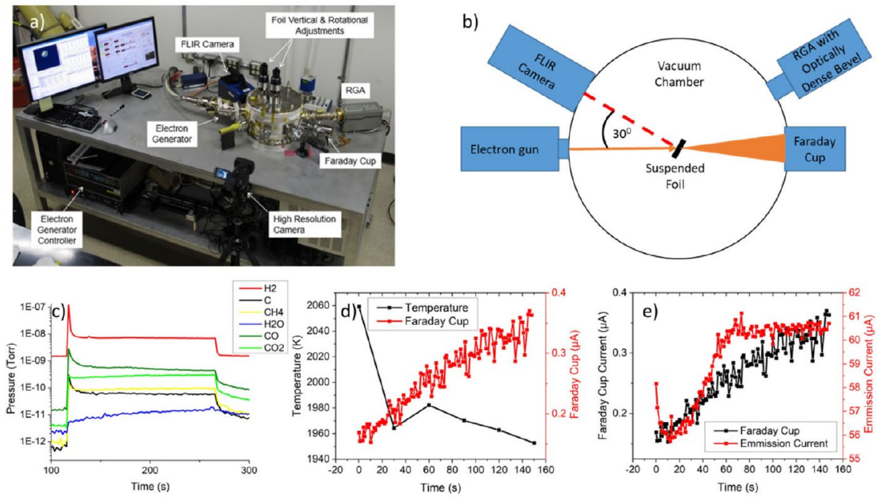

Fig. 1. (a) Photograph and (b) schematic of the Foil Test Stand. Example outputs from the (c) residual gas analyzer, (d) FLIR camera and Faraday cup, (e) Faraday cup and electron gun emission current.

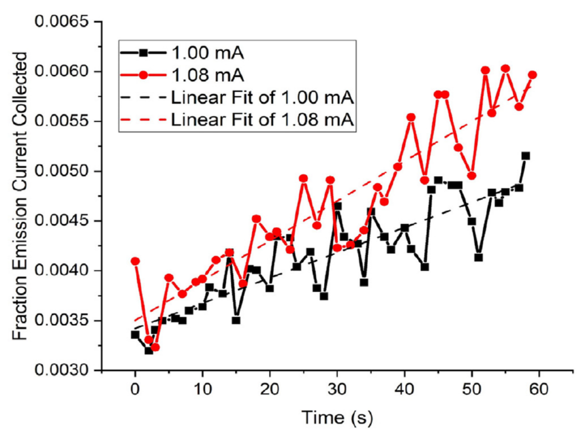

Fig. 2. Normalized Faraday cup current versus time demonstrating a steeper slope at higher emission current, which is indicative of a higher carbon sublimation rate.

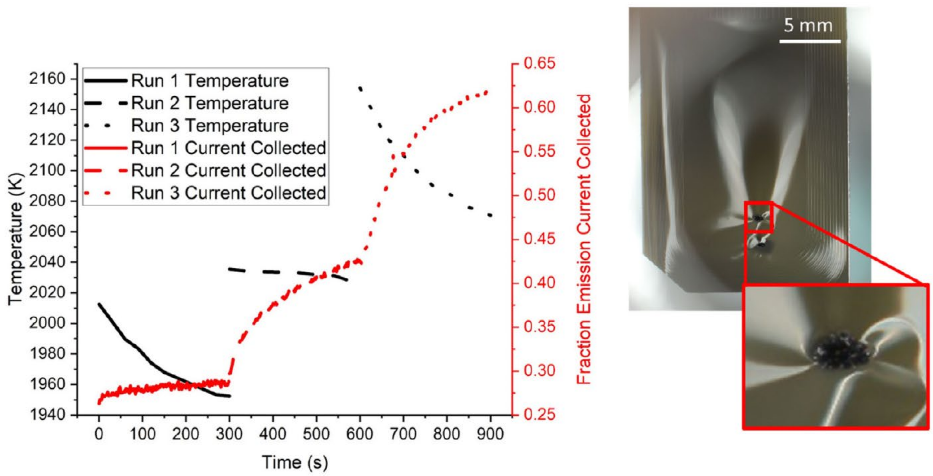

Fig. 3. (a) Temperature and normalized Faraday cup current versus time for 3 different runs (left). (b) Photograph of the foil after the 3 runs (right).

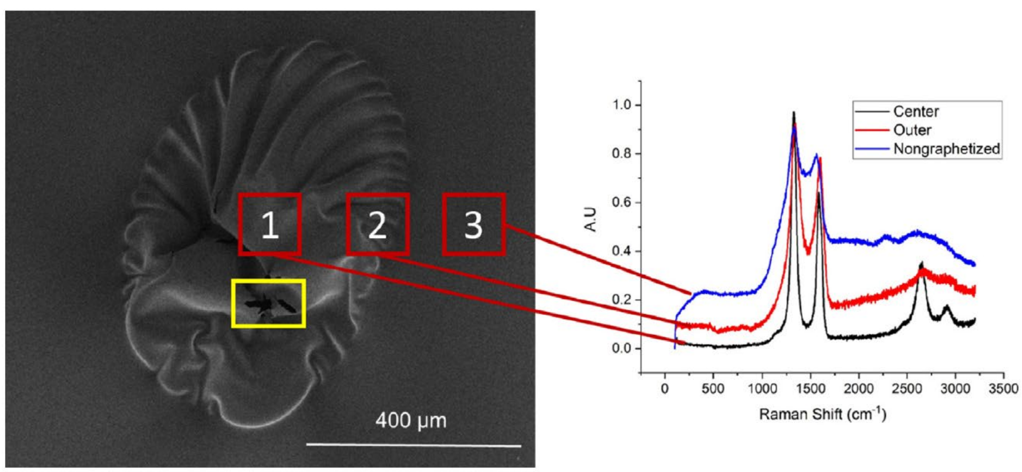

Fig. 4. SEM image of an exposed spot (left) and the corresponding Raman spectra (right). Example of holes in the foil (boxed in yellow).

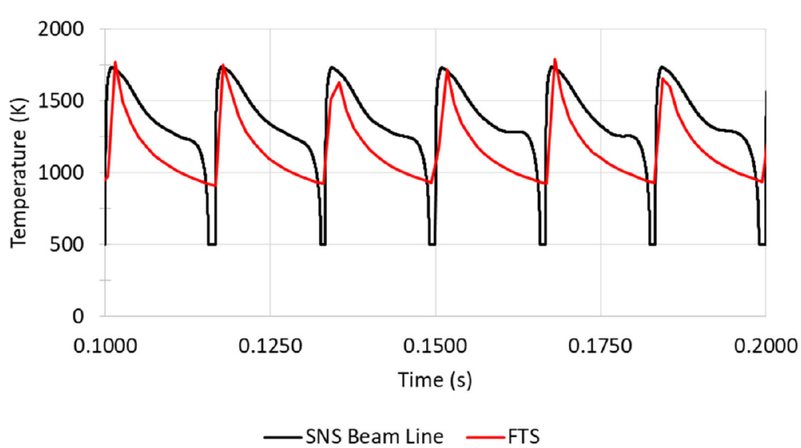

Fig. 5. Temperature data for the 1.4 MW, 1.0 GeV SNS beam (black) and the 750 μA FTS electron beam (red).. (For interpretation of the references to color in this figure legend, the reader is referred to the web version of this article.)

Table 1
Sensitivity analysis for COMSOL simulation parameters.

current	epsilon	ring radius	ring sigma	emmissivity	Thermal Conductivity	Peak T	Delta Peak T
μA		μm	μm		W/(m*K)	K	K
750	0.74	220	75	0.9	Normal	1801	0
825	0.74	220	75	0.9	Normal	1908	107
750	0.814	220	75	0.9	Normal	1908	107
750	0.74	242	75	0.9	Normal	1695	-106
750	0.74	220	82.5	0.9	Normal	1778	-23
750	0.74	220	75	0.99	Normal	1779	-22
750	0.74	220	75	0.9	1.1(Normal)	1779	-22

References

[1] F. Marti, P. Guetschow, E. Lansing, Y. Momozaki, J.A. Nolen, C.B. Reed, Development of a liquid lithium charge stripper for frib*, Heavy Ion Accel. Technol. Yokohama (2015) 134–138.
[2] C. Hojvat, M. Joy, R. Webber, Stripping foils for multiturn charge exchange, IEEE Trans. Nucl. Sci. NS-26 (1979) 4009–4011.
[3] S. Korenev, R. Dishman, A. Yebra, N. Meshcheryakov, I. Smirnov, I. Pavlovsky, R. Fink, Characterization of graphene stripper foils in 11-MeV cyclotrons, Phys. Procedia. 90 (2017) 369–373, http://dx.doi.org/10.1016/j.phpro.2017.09.034.
[4] R.W. Shaw, M.A. Plum, L.L. Wilson, C.F. Luck, A.G. McDermott, Y.J. Chen, R.L. Coleman, D.M. Gardner, C.S. Feigerle, T. Spickermann, M.J. Borden, Diamond stripper foil experience at SNS and PSR, in: EPAC 2008 - Contrib. to Proc, 2008, pp. 3563–3565.
[5] S.G. Lebedev, A.S. Lebedev, Calculation of the lifetimes of thin stripper targets under bombardment of intense pulsed ions, Phys. Rev. Spec. Top. Accel. Beams 11 (2008) 1–7, http://dx.doi.org/10.1103/PhysRevSTAB.11.020401.
[6] J.H. Kim, S.G. Hong, J.W. Kim, Y.G. Choi, Y.S. Kim, Investigation of cyclotron carbon foil lifetime in relation to its thickness, in: CYCLOTRONS 2013 - Proc. 20th Int. Conf. Cyclotrons Their Appl, 2014, pp. 227–229.
[7] Y. Takeda, M. Plum, O. Sns, O. Ridge, Thermal simulations of charge- exchange stripper foils for high-melting-point materials, in: IPAC 2013, 2013, pp. 3312–3314.
[8] W. Chou, M. Kostin, Z. Tang, Stripping efficiency and lifetime of carbon foils, Nucl. Instrum. Methods Phys. Res. A 590 (2008) 1–12, http://dx.doi.org/10. 1016/j.nima.2008.02.060.
[9] H.V. Smith, D.J. Adams, B. Jones, C.M. Warsop, Stripping foil simulations for ISIS injection upgrades, in: IPAC 2011-2nd Int. Part. Accel. Conf, 2011, pp. 3556–3558.
[10] C.J. Liaw, Y.Y. Lee, J. Alessi, J. Tuozzolo, Calculation of the maximum temperature on the carbon stripping foil of the spallation neutron source, in: IEEE Part. Accel. Conf., 1999, pp. 3300–3302, http://dx.doi.org/10.1109/pac.1999.792283.
[11] A. Rakhman, W. Blokland, Non-contact surface temperature measurements of nanocrystalline diamond foil under intense ion beams, in: M. Strojnik (Ed.), Infrared Remote Sens. Instrum. XXVIII, SPIE, 2020, pp. 77–83, http://dx.doi. org/10.1117/12.2568927.
[12] E.P. Barrowclough, C.S. Feigerle, C.F. Luck, L.L. Wilson, R.W. Shaw, M.A. Plum, Analysis of primary stripper foils at SNS by an electron beam foil test stand, in: 6th Int. Part. Accel. Conf. IPAC 2015, 2015, pp. 1230–1233.
[13] P.K. Saha, M. Yoshimoto, S. Hatakeyama, H. Hotchi, H. Harada, F. Tamura, K. Yamamoto, Y. Yamazaki, M. Kinsho, Y. Irie, First measurement and online monitoring of the stripper foil thinning and pinhole formation to achieve a longer foil lifetime in high-intensity accelerators, Phys. Rev. Accel. Beams 23 (2020) 82801, http://dx.doi.org/10.1103/PhysRevAccelBeams.23.082801.
[14] R.W. Shaw, D.P. Bontrager, L.L. Wilson, O. Ridge, C.S. Feigerle, C.F. Luck, M.A. Plum, S.N. Source, O. Ridge, An electron beam SNS foil test stand, in: Part. Accel. Conf., 2009, pp.1638–1640.
[15] L. Saturday, L. Wilson, S. Retterer, N.J. Evans, D. Briggs, P.D. Rack, N. Lavrik, Thermal conductivity of nano- and micro-crystalline diamond films studied by photothermal excitation of cantilever structures, Diam. Relat. Mater. 113 (2021) 108279, http://dx.doi.org/10.1016/j.diamond.2021.108279.
[16] E.P. Barrowclough, Analysis of Primary Stripper Foils at SNS By an Electron Beam Foil Test Stand, University of Tennessee, Knoxville, 2017.
[17] A. Shishlo, S. Cousineau, V. Danilov, J. Galambos, S. Henderson, J. Holmes, M. Plum, O. Ridge, The ORBIT simulation code: Benchmarking and applications, in: Proc ICAP 2006, 2006, pp. 53–58.
[18] D.M. Gruen, Nanocrystalline diamond films, Annu. Rev. Mater. Sci. 29 (1999) 211–259, http://dx.doi.org/10.1146/annurev.matsci.29.1.211.
[19] S. Prawer, R.J. Nemanich, Raman spectroscopy of diamond and doped diamond, Philos. Trans. R. Soc. A Math. Phys. Eng. Sci. 362 (2004) 2537–2565, http://dx.doi.org/10.1098/rsta.2004.1451.
[20] J.D. Fowlkes, R. Winkler, B.B. Lewis, M.G. Stanford, H. Plank, P.D. Rack, Simulation-guided 3D nanomanufacturing via focused electron beam induced de- position, ACS Nano. 10 (2016) 6163–6172, http://dx.doi.org/10.1021/acsnano. 6b02108.
[21] D.C. Joy, An introduction to Monte Carlo methods, Scanning Microsc. 5 (1991) 329–337, http://dx.doi.org/10.1016/j.physa.2014.06.014.
[22] M.J. Berger, J.S. Coursey, M. Zucker, J. Chang, Stopping-power & range tables for electrons, protons, and helium ions, NIST Stand. Ref. Database 124 (2017) http://dx.doi.org/10.18434/T4NC7P.
[23] COMSOL Multiphysics®, 2021, www.comsol.com.
[24] A.V. Khomich, V.G. Ralchenko, A.V. Vlasov, R.A. Khmelnitskiy, I.I. Vlasov, V.I. Konov, Effect of high temperature annealing on optical and thermal properties of CVD diamond, Diam. Relat. Mater 10 (2001) 546–551, http://dx.doi.org/10. 1016/S0925-9635(00)00517-3.
[25] E.P. Roth, R.D. Watson, M. Moss, W.D. Drotning, Thermophysical Properties of Advanced Carbon Materials For Tokamak Limiters, Albuquerque, New Mextico, 1989.
[26] A.C. Victor, Heat capacity of diamond at high temperatures, J. Chem. Phys. 36 (1962) 1903–1911, http://dx.doi.org/10.1063/1.1701288.
[27] R.R. Reeber, K. Wang, Thermal expansion, molar volume and specific heat of diamond from 0 to 3000K, J. Electron. Mater 25 (1996) 63–67, http://dx.doi. org/10.1007/BF02666175.
[28] A.A. Balandin, Thermal properties of graphene and nanostructured carbon materials, Nature Mater. 10 (2011) 569–581, http://dx.doi.org/10.1038/ nmat3064.
[29] R. Taylor, K.E. Gilchrist, L.J. Poston, in: N.Y. Carbon (Ed.), Thermal conductivity of polycrystalline graphite, 6, 1968, pp. 537–544, http://dx.doi.org/10.1016/0008-6223(68)90093-6.
[30] A.J. Bullen, K.E. O'Hara, D.G. Cahill, O. Monteiro, A. Von Keudell, Thermal conductivity of amorphous carbon thin films, J. Appl. Phys. 88 (2000) 6317–6320, http://dx.doi.org/10.1063/1.1314301.
[31] I. Pavlovsky, R.L. Fink, Graphene stripper foils, J. Vac. Sci. Technol. B, Nanotechnol. Microelectron. Mater. Process. Meas. Phenom. 30 (2012) 03D106, http://dx.doi.org/10.1116/1.3693594.
[32] K. Bogdanov, A. Fedorov, V. Osipov, T. Enoki, K. Takai, T. Hayashi, V. Ermakov, S. Moshkalev, A. Baranov, Annealing-induced structural changes of carbon onions: High-resolution transmission electron microscopy and Raman studies, 73, 2014, pp. 78–86, http://dx.doi.org/10.1016/j.carbon.2014.02.041,
[33] G. Gouadec, P. Colomban, Raman spectroscopy of nanomaterials: How spectra relate to disorder, particle size and mechanical

properties, Prog. Cryst. Growth Charact. Mater. 53 (2007) 1–56, http://dx.doi.org/10.1016/j.pcrysgrow.2007.01.001.
[34] J. Filik, J.N. Harvey, N.L. Allan, P.W. May, J.E.P. Dahl, S. Liu, R.M.K. Carlson, Raman spectroscopy of nanocrystalline diamond: An ab initio approach, Phys. Rev. B - Condens. Matter Mater. Phys. 74 (2006) 1–10, http://dx.doi.org/10.1103/PhysRevB.74.035423.
[35] W. Blokland, N. Evans, C. Luck, A. Rakhman, Injection foil temperature measurements at the SNS accelerator, in: HB2018 - Proc. 61st ICFA Adv. Beam Dyn. Work. High-Intensity High-Brightness Hadron Beams, 2018, pp. 104–109, http://dx.doi.org/10.18429/JACoW-HB2018-TUP2WE01.
[36] J. Park, K. Bae, T.R. Kim, C. Perez, A. Sood, M. Asheghi, K. Goodson, W. Park, Direct quantification of heat generation due to inelastic scattering of electrons using a nanocalorimeter, Adv. Sci 8, 2021, http://dx.doi.org/10.1002/ advs.202002876.
[37] P. Goldfinger, The vapor pressure and heat of sublimation of carbon, Symp. Combust. Flame Explos. Phenom. 3 (1948) 618–620, http://dx.doi.org/10.1016/S1062-2896(49)80084-5.

* Corresponding author.
E-mail address: lsaturda@vols.utk.edu (L. Saturday).

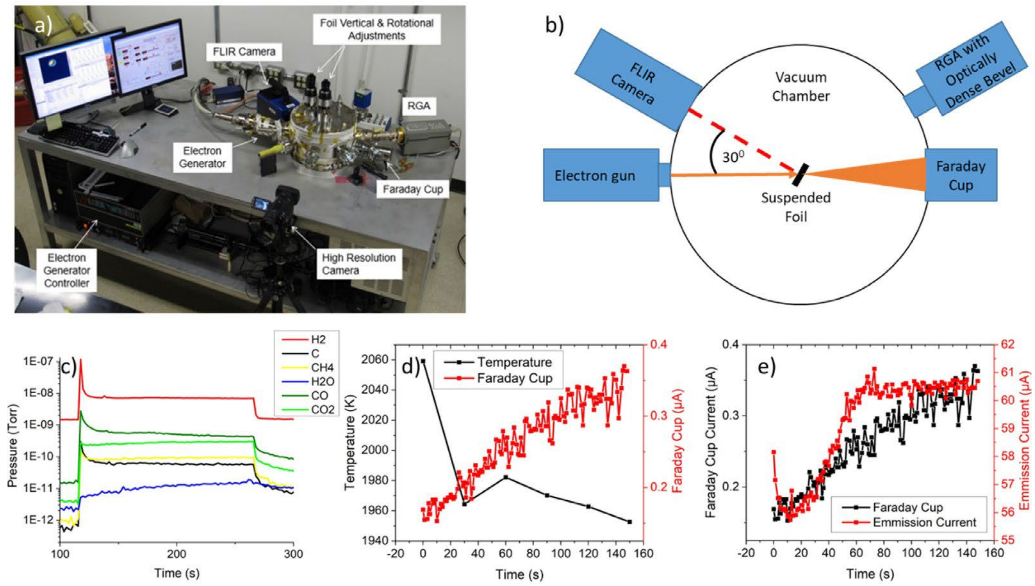

Fig. 1. (a) Photograph and (b) schematic of the Foil Test Stand. Example outputs from the (c) residual gas analyzer, (d) FLIR camera and Faraday cup, (e) Faraday cup and electron gun emission current.

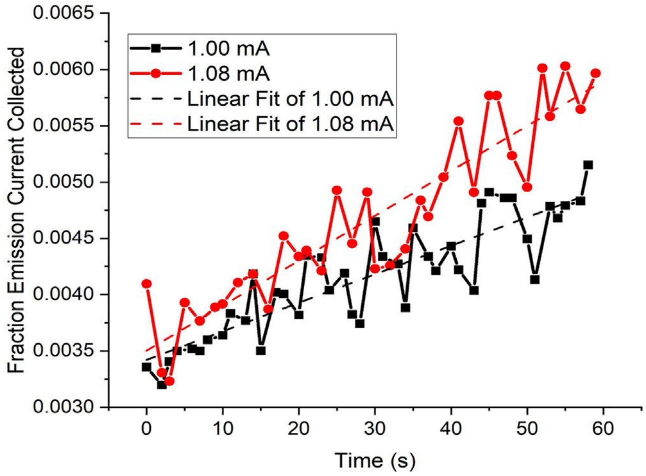

Fig. 2. Normalized Faraday cup current versus time demonstrating a steeper slope at higher emission current, which is indicative of a higher carbon sublimation rate.

during the second 300 s exposure begins to taper and nears saturation
at 600 s; the thinning in region 2 causes a net change of $\sim$65% in the normalized Faraday current and an $\sim$10 K decrease in temperature. In

$f\,(x, y) =$ $-2\sigma^2$

$x \quad + y$

$\sqrt{\quad}$ 2

x

(
exp

$$\left(\frac{2R\sqrt{x^2+y^2}-x^2-y^2-R^2}{2\sigma^2}\right)$$

$$-\exp\left(\frac{-2R\sqrt{x^2+y^2}-x^2-y^2-R^2}{2\sigma^2}\right)$$

the third region, the emission current is increased again to 380 μA, which causes an instantaneous increase of ~120 K in temperature. During the 300 s exposure the temperature decreases significantly (~90 K) concurrent with an increase in normalized Faraday cup current, indicating heavy sublimation and a potential hole formation in the film. Note the graphite vapor pressure is ~4 × 10^{-8} Torr at 2000 K, thus sublimation of the graphitized foil is reasonable in these electron exposure conditions. Fig. 3b shows the NCD foil after irradiation. The graphitized region can be clearly seen along with the deformations caused to the surrounding foil.

Post mortem testing was also conducted to elucidate the changes occurring to the nanocrystalline diamond foils. Emissivity measurements were conducted using a black body source as described in section 3.2.2.2 of Barrowclough's dissertation [16] and used for FLIR measurements. Raman spectra were taken in the relative regions shown in Fig. 4. The results show the central area 1 has sharp peaks at 1325 and 1585 cm^{-1}, which are associated with strong crystalline graphite and diamond vibrations, respectively. Additionally, peaks around 2700 and 2900 cm^{-1} are observed and are similar to peak patterns found in carbon nano-onions [32]. The second region has discernible peaks at 1335 and 1595 cm^{-1} which are broader than region 1, suggestive of potentially a more disordered material with defects [33] or a shift to smaller grain size of the sample [34]. Region 3 is an unexposed region and has two peaks at 1330 and 1565 cm^{-1}; the peaks are broad and indicative of the nanocrystalline diamond and an amorphous phase of carbon. Additionally, SEM imaging was conducted on these foils in order to directly observe potential failures and can be seen in Fig. 4. Holes in the foil caused during exposure are seen in the SEM images. This helps to determine that the cause of the failure is sublimation rather than mechanical failure. Hole formation, noted in the yellow box in Fig. 4 SEM, is attributed to excessive sublimation at the hot spots

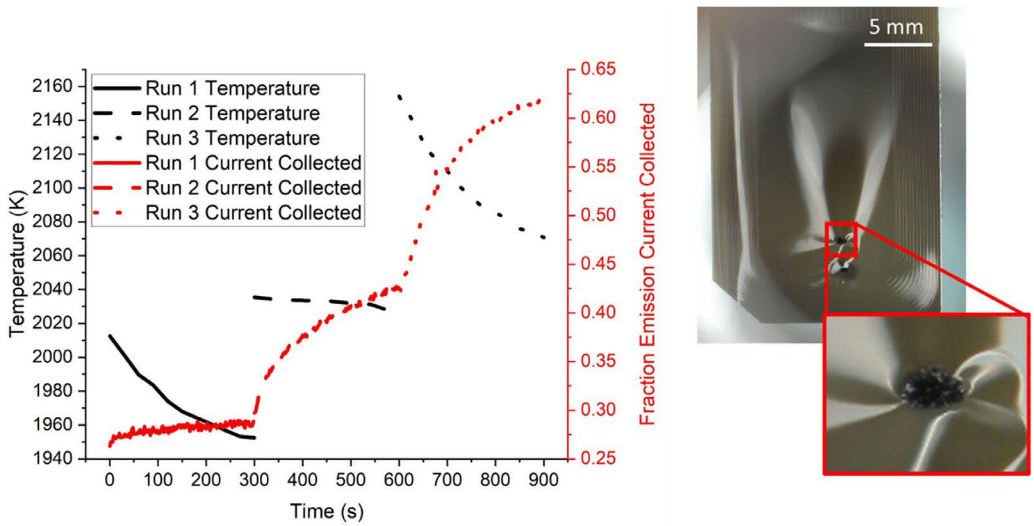

Fig. 3. (a) Temperature and normalized Faraday cup current versus time for 3 different runs (left). (b) Photograph of the foil after the 3 runs (right).

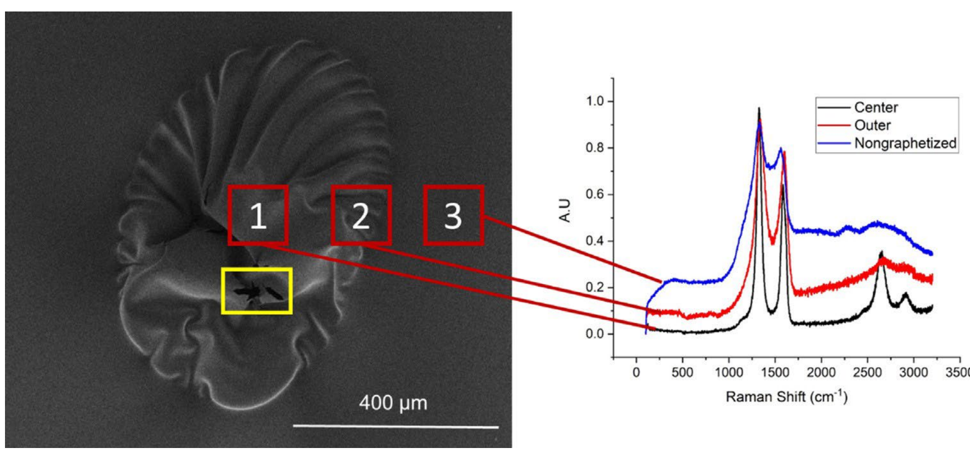

Fig. 4. SEM image of an exposed spot (left) and the corresponding Raman spectra (right). Example of holes in the foil (boxed in yellow).

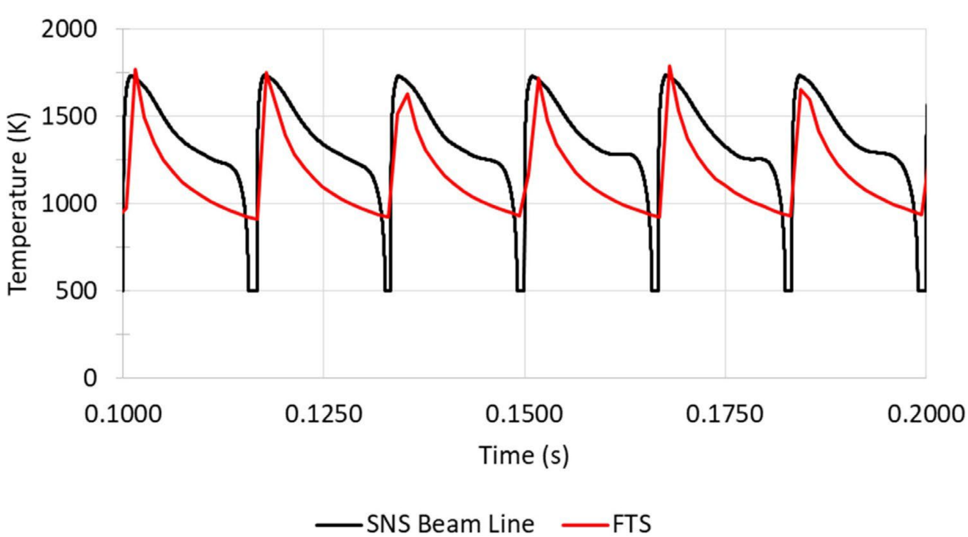

Fig. 5. Temperature data for the 1.4 MW, 1.0 GeV SNS beam (black) and the 750 μA FTS electron beam (red).. (For interpretation of the references to color in this figure legend, the reader is referred to the web version of this article.)

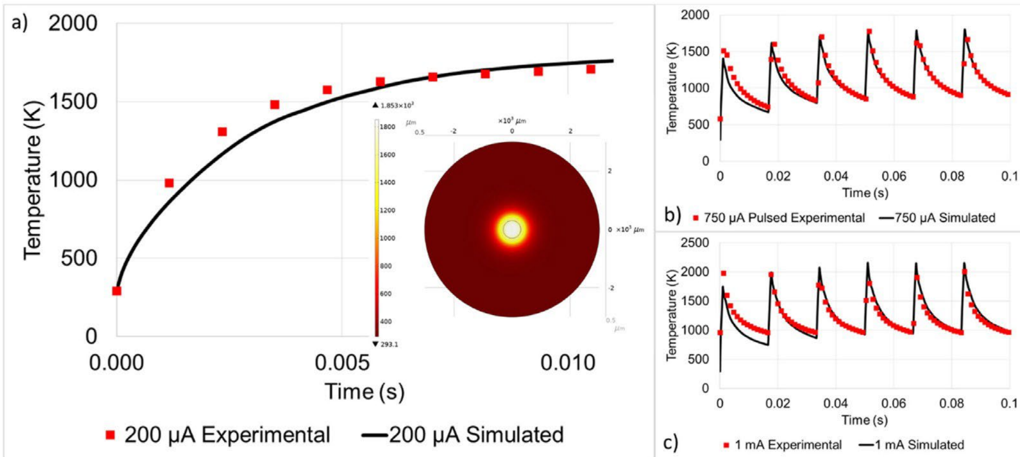

Fig. 6. (A) 200 µA continuous electron beam experimental and simulated comparisons. Inset graph shows simulated heat profile on foil. (B) 750 µA pulsed electron beam experimental and simulated data. (C) 1 mA pulsed electron beam experimental and simulated data.

Table 1
Sensitivity analysis for COMSOL simulation parameters.

current	epsilon	ring radius	ring sigma	emmissivity	Thermal Conductivity	Peak T	Delta Peak T
µA		µm	µm		W/(m*K)	K	K
750	0.74	220	75	0.9	Normal	1801	0
825	0.74	220	75	0.9	Normal	1908	107
750	0.814	220	75	0.9	Normal	1908	107
750	0.74	242	75	0.9	Normal	1695	-106
750	0.74	220	82.5	0.9	Normal	1778	-23
750	0.74	220	75	0.99	Normal	1779	-22
750	0.74	220	75	0.9	1.1(Normal)	1779	-22

1. Conclusion

CRediT authorship contribution statement

Leo Saturday: Methodology, Investigation, Formal analysis, Visu- alization, Writing – original draft. **Chris Luck:** Methodology, Inves- tigation, Visualization. **Leslie Wilson:** Resources. **Jason D. Fowlkes:** Software. **Philip D. Rack:** Conceptualization, Supervision, Writing – review & editing. **Nicholas J. Evans:** Conceptualization, Supervision, Writing – review & editing, Formal analysis, Funding acquisition.

Declaration of competing interest

The authors declare that they have no known competing finan- cial interests or personal relationships that could have appeared to influence the work reported in this paper.

Acknowledgments

This work was supported by the DOE office of Science User Facili- ties. LS, LW, and NE are supported through funding for the Spallation Neutron Source. SNS is managed by UT-Battelle, LLC, under contract DE- AC05-00OR22725 for the U.S. Department of Energy. Foil synthe- sis, certain post-mortem testing, and modeling were conducted at the Center for Nanophase Materials Sciences, which is also a DOE Office of Science User Facility. Additionally, the authors would like to thank Jeff Holmes for simulations of the SNS beam/foil interaction, and Willem Blokland for operational data from the SNS foil pyrometer.

Appendix A. Supplementary data

Supplementary material related to this article can be found online at https://doi.org/10.1016/j.nima.2021.166226.

References

[1] F. Marti, P. Guetschow, E. Lansing, Y. Momozaki, J.A. Nolen, C.B. Reed, Development of a liquid lithium charge stripper for frib*, Heavy Ion Accel. Technol. Yokohama (2015) 134–138.

[2] C. Hojvat, M. Joy, R. Webber, Stripping foils for multiturn charge exchange, IEEE Trans. Nucl. Sci. NS-26 (1979) 4009–4011.

[3] S. Korenev, R. Dishman, A. Yebra, N. Meshcheryakov, I. Smirnov, I. Pavlovsky, R. Fink, Characterization of graphene stripper foils in 11-MeV cyclotrons, Phys. Procedia. 90 (2017) 369–373, http://dx.doi.org/10.1016/j.phpro.2017.09.034.

[4] R.W. Shaw, M.A. Plum, L.L. Wilson, C.F. Luck, A.G. McDermott, Y.J. Chen, R.L. Coleman, D.M. Gardner, C.S. Feigerle, T. Spickermann, M.J. Borden, Diamond stripper foil experience at SNS and PSR, in: EPAC 2008 - Contrib. to Proc, 2008, pp. 3563–3565.

[5] S.G. Lebedev, A.S. Lebedev, Calculation of the lifetimes of thin stripper targets under bombardment of intense pulsed ions, Phys. Rev. Spec. Top. Accel. Beams 11 (2008) 1–7, http://dx.doi.org/10.1103/PhysRevSTAB.11.020401.

[6] J.H. Kim, S.G. Hong, J.W. Kim, Y.G. Choi, Y.S. Kim, Investigation of cyclotron carbon foil lifetime in relation to its thickness, in: CYCLOTRONS 2013 - Proc. 20th Int. Conf. Cyclotrons Their Appl, 2014, pp. 227–229.
[7] Y. Takeda, M. Plum, O. Sns, O. Ridge, Thermal simulations of charge- exchange stripper foils for high-melting-point materials, in: IPAC 2013, 2013, pp. 3312–3314.
[8] W. Chou, M. Kostin, Z. Tang, Stripping efficiency and lifetime of carbon foils, Nucl. Instrum. Methods Phys. Res. A 590 (2008) 1–12, http://dx.doi.org/10.1016/j.nima.2008.02.060.
[9] H.V. Smith, D.J. Adams, B. Jones, C.M. Warsop, Stripping foil simulations for ISIS injection upgrades, in: IPAC 2011-2nd Int. Part. Accel. Conf, 2011, pp. 3556–3558.
[10] C.J. Liaw, Y.Y. Lee, J. Alessi, J. Tuozzolo, Calculation of the maximum tempera- ture on the carbon stripping foil of the spallation neutron source, in: IEEE Part. Accel. Conf., 1999, pp. 3300–3302, http://dx.doi.org/10.1109/pac.1999.792283.
[11] A. Rakhman, W. Blokland, Non-contact surface temperature measurements of nanocrystalline diamond foil under intense ion beams, in: M. Strojnik (Ed.), Infrared Remote Sens. Instrum. XXVIII, SPIE, 2020, pp. 77–83, http://dx.doi. org/10.1117/12.2568927.
[12] E.P. Barrowclough, C.S. Feigerle, C.F. Luck, L.L. Wilson, R.W. Shaw, M.A. Plum, Analysis of primary stripper foils at SNS by an electron beam foil test stand, in: 6th Int. Part. Accel. Conf. IPAC 2015, 2015, pp. 1230–1233.
[13] P.K. Saha, M. Yoshimoto, S. Hatakeyama, H. Hotchi, H. Harada, F. Tamura, K. Yamamoto, Y. Yamazaki, M. Kinsho, Y. Irie, First measurement and online monitoring of the stripper foil thinning and pinhole formation to achieve a longer foil lifetime in high-intensity accelerators, Phys. Rev. Accel. Beams 23 (2020) 82801, http://dx.doi.org/10.1103/PhysRevAccelBeams.23.082801.
[14] R.W. Shaw, D.P. Bontrager, L.L. Wilson, O. Ridge, C.S. Feigerle, C.F. Luck, M.A. Plum, S.N. Source, O. Ridge, An electron beam SNS foil test stand, in: Part. Accel. Conf., 2009, pp. 1638–1640.
[15] L. Saturday, L. Wilson, S. Retterer, N.J. Evans, D. Briggs, P.D. Rack, N. Lavrik, Thermal conductivity of nano- and micro-crystalline diamond films studied by photothermal excitation of cantilever structures, Diam. Relat. Mater. 113 (2021) 108279, http://dx.doi.org/10.1016/j.diamond.2021.108279.
[16] E.P. Barrowclough, Analysis of Primary Stripper Foils at SNS By an Electron Beam Foil Test Stand, University of Tennessee, Knoxville, 2017.
[17] A. Shishlo, S. Cousineau, V. Danilov, J. Galambos, S. Henderson, J. Holmes, M. Plum, O. Ridge, The ORBIT simulation code: Benchmarking and applications, in: Proc ICAP 2006, 2006, pp. 53–58.
[18] D.M. Gruen, Nanocrystalline diamond films, Annu. Rev. Mater. Sci. 29 (1999) 211–259, http://dx.doi.org/10.1146/annurev.matsci.29.1.211.
[19] S. Prawer, R.J. Nemanich, Raman spectroscopy of diamond and doped diamond, Philos. Trans. R. Soc. A Math. Phys. Eng. Sci. 362 (2004) 2537–2565, http://dx.doi.org/10.1098/rsta.2004.1451.
[20] J.D. Fowlkes, R. Winkler, B.B. Lewis, M.G. Stanford, H. Plank, P.D. Rack, Simulation-guided 3D nanomanufacturing via focused electron beam induced de- position, ACS Nano. 10 (2016) 6163–6172, http://dx.doi.org/10.1021/acsnano. 6b02108.
[21] D.C. Joy, An introduction to Monte Carlo methods, Scanning Microsc. 5 (1991) 329–337, http://dx.doi.org/10.1016/j.physa.2014.06.014.
[22] M.J. Berger, J.S. Coursey, M. Zucker, J. Chang, Stopping-power & range tables for electrons, protons, and helium ions, NIST Stand. Ref. Database 124 (2017) http://dx.doi.org/10.18434/T4NC7P.
[23] COMSOL Multiphysics®, 2021, www.comsol.com.
[24] A.V. Khomich, V.G. Ralchenko, A.V. Vlasov, R.A. Khmelnitskiy, I.I. Vlasov, V.I. Konov, Effect of high temperature annealing on optical and thermal properties of CVD diamond, Diam. Relat. Mater 10 (2001) 546–551, http://dx.doi.org/10. 1016/S0925-9635(00)00517-3.
[25] E.P. Roth, R.D. Watson, M. Moss, W.D. Drotning, Thermophysical Properties of Advanced Carbon Materials For Tokamak Limiters, Albuquerque, New Mextico, 1989.
[26] A.C. Victor, Heat capacity of diamond at high temperatures, J. Chem. Phys. 36 (1962) 1903–1911, http://dx.doi.org/10.1063/1.1701288.
[27] R.R. Reeber, K. Wang, Thermal expansion, molar volume and specific heat of diamond from 0 to 3000K, J. Electron. Mater 25 (1996) 63–67, http://dx.doi.org/10.1007/BF02666175.
[28] A.A. Balandin, Thermal properties of graphene and nanostructured car- bon materials, Nature Mater. 10 (2011) 569–581, http://dx.doi.org/10.1038/ nmat3064.
[29] R. Taylor, K.E. Gilchrist, L.J. Poston, in: N.Y. Carbon (Ed.), Thermal conductivity of polycrystalline graphite, 6, 1968, pp. 537–544, http://dx.doi.org/10.1016/0008-6223(68)90093-6.
[30] A.J. Bullen, K.E. O'Hara, D.G. Cahill, O. Monteiro, A. Von Keudell, Thermal con- ductivity of amorphous carbon thin films, J. Appl. Phys. 88 (2000) 6317–6320, http://dx.doi.org/10.1063/1.1314301.
[31] I. Pavlovsky, R.L. Fink, Graphene stripper foils, J. Vac. Sci. Technol. B, Nan- otechnol. Microelectron. Mater. Process. Meas. Phenom. 30 (2012) 03D106, http://dx.doi.org/10.1116/1.3693594.

[32] K. Bogdanov, A. Fedorov, V. Osipov, T. Enoki, K. Takai, T. Hayashi, V. Ermakov, S. Moshkalev, A. Baranov, Annealing-induced structural changes of carbon onions: High-resolution transmission electron microscopy and Raman studies, 73, 2014, pp. 78–86, http://dx.doi.org/10.1016/j.carbon.2014.02.041,

[33] G. Gouadec, P. Colomban, Raman spectroscopy of nanomaterials: How spectra relate to disorder, particle size and mechanical properties, Prog. Cryst. Growth Charact. Mater. 53 (2007) 1–56, http://dx.doi.org/10.1016/j.pcrysgrow.2007.01.001.

[34] J. Filik, J.N. Harvey, N.L. Allan, P.W. May, J.E.P. Dahl, S. Liu, R.M.K. Carlson, Raman spectroscopy of nanocrystalline diamond: An ab initio approach, Phys. Rev. B - Condens. Matter Mater. Phys. 74 (2006) 1–10, http://dx.doi.org/10.1103/PhysRevB.74.035423.

[35] W. Blokland, N. Evans, C. Luck, A. Rakhman, Injection foil temperature measurements at the SNS accelerator, in: HB2018 - Proc. 61st ICFA Adv. Beam Dyn. Work. High-Intensity High-Brightness Hadron Beams, 2018, pp. 104–109, http://dx.doi.org/10.18429/JACoW-HB2018-TUP2WE01.

[36] J. Park, K. Bae, T.R. Kim, C. Perez, A. Sood, M. Asheghi, K. Goodson, W. Park, Direct quantification of heat generation due to inelastic scattering of electrons using a nanocalorimeter, Adv. Sci 8, 2021, http://dx.doi.org/10.1002/advs.202002876.

[37] P. Goldfinger, The vapor pressure and heat of sublimation of carbon, Symp. Combust. Flame Explos. Phenom. 3 (1948) 618–620, http://dx.doi.org/10.1016/S1062-2896(49)80084-5.